


PSFC/JA-02-7

Ion Collection by a Sphere in a Flowing Plasma:

1. Quasineutral

View metadata, citation and similar papers at core.ac.uk

brought to you by  **COR**

provided by DSpace@M

I.H. Hutchinson

June 2002

Plasma Science and Fusion Center
Massachusetts Institute of Technology
Cambridge, MA 02139 USA

This work was supported by the U.S. Department of Energy, Cooperative Grant No. DE-FC02-99ER54512. Reproduction, translation, publication, use and disposal, in whole or in part, by or for the United States government is permitted.

Submitted for publication to *Plasma Physics and Controlled Fusion*.

Ion Collection by a Sphere in a Flowing Plasma: 1. Quasineutral

I. H. Hutchinson

Plasma Science and Fusion Center
Massachusetts Institute of Technology
Cambridge, MA, USA

Abstract

The spatial distribution of collisionless ions collected by a spherical object of radius much larger than the Debye length, in a flowing plasma, is calculated using a particle-in-cell code. The results provide the first rigorous theoretical calibration of a “Mach probe” in a plasma with negligible magnetic field. They are also applicable, for example, to spacecraft-plasma interactions. Ion to electron temperature ratios $0.1 < T_i/ZT_e < 10$ are explored. Qualitative differences are observed between the results for low and high T_i/ZT_e , arising from ion dynamics in the wake. However, a practically universal form for the upstream to downstream current density dependence on flow velocity is observed for $T_i/ZT_e \lesssim 3$.

1 Introduction

A sphere in a stationary collisionless plasma is arguably the simplest possible problem involving a bounded object in a plasma. The classic assumption is that the surface simply removes ions (and electrons) incident on it, by neutralization. In addition, if the total current density to the surface is small relative to the random electron current, for example if it is floating, a good approximation is to assume that the surface acquires a sufficiently negative potential as to reflect most electrons, and hence that the electrons adopt a thermal Boltzmann density distribution proportional to $\exp(e\phi/T_e)$, where e is the electron charge, and ϕ the electric potential. Despite its simplicity, and despite earlier partial or approximate analyses [1, 2, 3, 4, 5], this problem was not definitively solved for non-zero ion temperature until the 1960s. The quasineutral case with negligible Debye length compared with the sphere radius was solved for $T_i/T_e = 1$ by Al’pert et al [6]. The problem with finite Debye length was also definitively explored at almost the same time by Laframboise [7]. These solutions, based on kinetic theory and detailed particle orbit analysis, used [5] the fact that angular momentum is conserved in this spherically symmetric situation. This allows a major simplification, but even so the analysis and numerical methods required for the integro-differential problem were, and are, challenging. Perhaps this difficulty and the relative comprehensiveness of

Laframboise's results, have discouraged all but a few [8, 9] substantial elaborations of this problem, even though some subtle questions remain about the limit of zero temperature and collisionality [10, 7].

Adding a background plasma flow, or equivalently a motion of the sphere through a stationary plasma, breaks the symmetry of the problem and undermines the previous analysis approach, because angular momentum is no longer conserved. This asymmetric problem gained early attention mostly for applications to spacecraft in the ionosphere (see e.g. [6]), which generally move at substantially supersonic speeds. Many analyses assume that such situations are adequately treated by ignoring the effect of the self-consistent electric field on the ion orbits. However, that approach does not yield the correct structure of the plasma wake, and can be expected to give approximately correct ion collection only if $T_i/ZT_e \gg 1$, which is very rare in nature. In the limit of large flow velocity relative to the sound speed, more satisfactory approximations are to ignore only the *parallel* electric field and velocity spread, yielding tractable equations, with self-similar solutions, for the perpendicular velocity distribution [11, 12] in the wake. However, those approximations disqualify the analysis from calculating the ion flux to the sphere in the wake, even in cases where the structure of the far wake is correctly obtained. Even the more recent numerical studies that include more self consistent physics [13] give no information about the ion collection, possibly because the downstream flux is so small for highly supersonic flow. In many studies, modeling results are very specific to particular experiments (e.g.[14]).

An application of comparable current importance in plasmas for fusion and industrial processing applications is to measure the plasma flow by measuring separately the upstream and downstream ion collection currents to electrically distinct conductors. The various forms of such measurements are often called Mach probes. The calibration of Mach probes in *magnetized* plasmas (that is, when the ion Larmor radius is smaller than the probe dimension) has been established by theory [15, 16] and verified in experiments [17]. But, remarkably, the simpler-seeming problem of unmagnetized Mach probes, which is the subject of the present study, and especially the relationship between the upstream/downstream current ratio and the flow velocity has not till now been satisfactorily solved. Calibration formulas by Hudis and Lidsky, based on heuristic arguments [18] have recently been increasingly used, for want of anything better, since experiments badly need some calibration (see e.g. [19, 20, 21, 22]). However, as has recently been pointed out [23], the physical inconsistencies of the Hudis and Lidsky arguments provide no confidence that they are correct. Indeed, the results of the present work demonstrate that they are quantitatively as well as physically in error.

Yet another application is in calculating the charging of grains in dusty plasmas. That generally involves large Debye length relative to sphere size, to which the present quasi-neutral results are not applicable.

This paper reports an essentially fully consistent solution of the flowing collisionless plasma and sphere problem, with the only approximations being that the electrons are governed by a Boltzmann factor and that the Debye length, λ_D is infinitesimally small. A future publication will address non-zero λ_D , but the present quasineutral case has the merit that the ion collection flux density is independent of the probe potential, ϕ_0 , so that the results depend on two fewer parameters (λ_D/R and ϕ_0) than otherwise, and can be expressed more compactly. It also has the merit that it represents the limit in which probes

are easiest to interpret.

The calculations are performed using a particle-in-cell computer code written specifically for this problem in spherical coordinates, dubbed SCEPTIC (Specialized-Coordinate Electrostatic Particle and Thermals In Cell). In the next section this code is described, and in section 3 it is benchmarked against prior solutions for stationary plasmas. The main results of the present work are presented in section 4 and compared with previous assumptions and experiments in section 5.

2 Equations and Methods

Each ion, of charge Ze and mass m , at position \mathbf{x} is governed by Newton's law in the electrostatic potential:

$$m \frac{d^2 \mathbf{x}}{dt^2} = -Ze \nabla \phi. \quad (1)$$

The electrons have density

$$n_e = Zn_{i\infty} \exp(e\phi/T_e), \quad (2)$$

where $n_{i\infty}$ is the ion density where $\phi = 0$, far from the probe. The self consistent potential satisfies Poisson's equation. In the present approximation that the Debye length is negligibly small compared with the radius of the probe, Poisson's equation may be replaced by the equation of quasineutrality, which eliminates the electron density from the problem,

$$n_i = n_e/Z = n_{i\infty} \exp(e\phi/T_e). \quad (3)$$

The ion density n_i is obtained by integration over all velocities of the ion distribution function, $f(\mathbf{x}, \mathbf{v})$.

It is convenient to measure potential in units of T_e/e , velocity in units of $(ZT_e/m)^{1/2}$, density in units of $n_{i\infty}$ and to take the probe radius as $r = 1$, effectively making the units of time equal to the probe radius divided by $(ZT_e/m)^{1/2}$. These choices non-dimensionalize the problem, but for simplicity, we shall continue to use the same symbols for the dimensionless quantities. Notice that the velocity is normalized to a value that is somewhat less than the ion sound speed ($c_s = [(ZT_e + 3T_i)/m]^{1/2}$) when the ion temperature is non-zero. But the normalization factor $(ZT_e/m)^{1/2}$ is well defined and independent of position, unlike T_i .

2.1 Mesh and Difference Scheme

The particle-in-cell (PIC) computational method[24, 25] derives the ion distribution by solving eq (1) for a large number of individual particles spanning the distribution function, and assigning their charges to a mesh of cells on which the electric potential is calculated. The SCEPTIC code uses either nearest grid point (NGP) or linearly interpolated (cloud in cell, CIC) assignment of charges[25]. Unlike most PIC codes, the mesh here is chosen as a spherical grid with equal spacing in radius (r) and in the cosine of the azimuthal angle (θ) relative to the direction of flow. The grid is two-dimensional in space, the system being assumed rotationally symmetric about the direction of flow (z). In other words, there are considered to be only a single cell and no gradients in the angle of longitude.

Particles (ions) are represented, and equation (1) is solved, in all three cartesian coordinates for position and velocity (6-dimensional phase space) using the appropriate components of radial and angular acceleration derived from $\partial\phi/\partial r$ and $\partial\phi/\partial\theta$. The cartesian particle representation proves to be more satisfactory than spherical because it avoids coordinate singularities at which numerical difficulties are otherwise experienced. It incurs a significant computational cost in converting particle to cell position and acceleration components, but this cost is no more than half the total. Standard leap-frog integration [25] is used for the particle advance.

The PIC computational method faces a trade-off. To reduce random noise one would like to have a large number of particles per cell, but to resolve features of small spatial scale one would like to have small cells, and so one is forced to a large total number of particles, which is limited by computational resources. The difficulty of this trade-off becomes particularly acute at the probe surface $r = 1$, because the quasineutral equations experience a square-root slope singularity there, necessary to match their solution to the (infinitesimally thin and not specifically modelled) sheath. At the same place, the mesh cells are smallest in peripheral extent, because the radius is smallest, and the plasma density is also smallest because the potential is at its most negative. The expedient used in fluid codes to resolve the singularity, namely to employ a mesh that is spaced uniformly in a coordinate proportional to the square-root of the distance from the sheath edge [15], is inappropriate for a PIC code, because it leads to too few particles per cell near the boundary. In practice, a uniform mesh spacing in r is a reasonable compromise.

If one chooses a standard mesh interpolation scheme[25] for the radial force, then the result of being unable to use extremely fine spacing at the sheath edge is to obtain only square-root accuracy in the calculation. However, it is possible to interpolate the radial force in such a way as to take into account the knowledge that the sheath-edge possesses a square-root singularity and thereby obtain far more accurate results without excessive cells and particles. This process uses an alternative radial coordinate proportional to the square-root of the distance from the sheath edge,

$$\zeta \equiv \sqrt{2(r-1)}, \quad (4)$$

so that

$$\frac{\partial\phi}{\partial r} = \frac{1}{\zeta} \frac{\partial\phi}{\partial\zeta}, \quad (5)$$

but mesh spacing that is, of course, non-uniform in ζ -space, because uniform in r . At the sheath boundary, $\partial\phi/\partial\zeta$ tends to a finite value. All the singularity in $\partial\phi/\partial r$ is contained in the term $1/\zeta$. Therefore, when taking finite differences to approximate the gradient, if this is done in ζ -space, at least linear accuracy can be obtained. The consistent scheme adopted is then to attribute the finite difference approximation

$$\frac{\partial\phi}{\partial\zeta} = \frac{\phi_{i+1} - \phi_i}{\zeta_{i+1} - \zeta_i} \quad (6)$$

to the position

$$\zeta_{i+1/2} \equiv (\zeta_i + \zeta_{i+1})/2. \quad (7)$$

The value of the radial acceleration, $\partial\phi/\partial r$ is then obtained for each particle based on appropriate choice of interpolation of $\partial\phi/\partial\zeta$ from the points $\zeta_{i+1/2}$, for example linear interpolation or nearest grid point, followed by division by the *exact* local value of ζ at the particle. The field singularity at the sheath edge is thereby reproduced even though the mesh itself does not resolve it.

The use of this radial force interpolation scheme does not conserve momentum for the PIC simulation, which is a problem widely discussed in the literature [25, 24]. However, for the present problem that is a minor factor compared with approximating the acceleration at the sheath edge.

2.2 Boundary Conditions

Particle trajectories are advanced until they cross a boundary of the computational domain, either at the sphere, $r = 1$, or at an outer boundary $r = r_{\max}$ chosen far enough from the probe so that its finite distance is unimportant, but not so far that the simulation volume overwhelms our computational resources. Typically $r_{\max} = 5$. A constant number of particles is maintained by immediately reinjecting from the outer boundary, any particle that leaves the domain. Particles are reinjected with random position on the outer boundary and random velocity. The probability distribution of position and velocity is chosen proportional to the differential flux of particles across the boundary arising from a shifted Maxwellian distribution, our choice for the unperturbed ion distribution function, as follows.

The background (normalized) distribution function is taken as a Maxwellian shifted by a flow velocity v_f in the z -direction. At an azimuthal angle θ the inward radial component of the drift velocity is $v_{fr} = -v_f \cos\theta$ and the cumulative distribution of inward traveling particles, integrated over all tangential velocities is

$$\begin{aligned} G(u, \cos\theta) &= \frac{1}{\sqrt{2\pi}} \int_0^{-u} u' \exp[-(u' - u_{fr})^2/2] du' & (8) \\ &= \frac{1}{\sqrt{2\pi}} \left[\exp\left(-\frac{u_{fr}^2}{2}\right) - \exp\left(-\frac{(u - u_{fr})^2}{2}\right) \right] \\ &\quad + \frac{u_{fr}}{2} \left[\operatorname{erf}\left(\frac{u - u_{fr}}{\sqrt{2}}\right) - \operatorname{erf}\left(-\frac{u_{fr}}{\sqrt{2}}\right) \right] & (9) \end{aligned}$$

Here we are using u to denote the (r -component of) velocity normalized to the ion thermal velocity: $u = v/(T_i/m)^{1/2}$, and the dependence on $\cos\theta$ is implicit in $u_{fr} = u_f \cos\theta$.

In the limit $u \rightarrow \infty$ this becomes

$$G(\infty, \cos\theta) = \frac{1}{\sqrt{2\pi}} \exp\left(-\frac{u_{fr}^2}{2}\right) + \frac{u_{fr}}{2} \left[\operatorname{erfc}\left(-\frac{u_{fr}}{\sqrt{2}}\right) \right] \quad (10)$$

which is the differential distribution of total flux with respect to $\cos\theta$. From that we can obtain the cumulative distribution in $\cos\theta$ which we denote

$$Q(\cos\theta) = \int_{-1}^{\cos\theta} G(\infty, \cos\theta') d\cos\theta'. \quad (11)$$

The functions $Q(\cos \theta)$ and $G(u, \cos \theta)$ are precalculated over a sufficiently fine mesh spanning the domain of their arguments. Then the random deviates appropriately distributed are found by (1) obtaining two independent uniform random deviates ξ_1, ξ_2 over the range $0 < \xi < 1$; (2) solving the equation $Q(\cos \theta) = \xi_1 Q(1)$ to determine $\cos \theta$; (3) with this value of $\cos \theta$, solving $G(u, \cos \theta) = \xi_2 G(\infty, \cos \theta)$ to find u , the radial velocity; (4) choosing the tangential velocities from two Gaussian distributions, the azimuthal distribution shifted by $u_f \sin \theta$.

Since the number of particles is what is fixed, the particle density at infinity is not known a priori. Therefore the reference value of potential is unknown until the calculation is converged. This does not affect the dynamics, since it is only the potential *gradient* that matters. Therefore the calculation is carried out with the potential determined simply from $\phi = \ln n_i$. When the result is converged, the density is rescaled to be unity at infinity. The scaling factor is determined by fitting a value and a slope to the solution averaged over all angles ($\cos \theta \leq 0$) in the outer 40% of radius, and using the asymptotic form $(n_\infty - n) \propto 1/r^2$, which is known for the stationary plasma case [5] and gives excellent consistency for finite flow cases, where the upstream density is hardly perturbed.

The cells at the boundaries of the calculation domain require special treatment of the finite differences to enable field values to be obtained all the way to the cell edge. For the outer boundary the extrapolation used is $\partial\phi/\partial\zeta = \text{const.}$ The more consistent alternative $\partial \ln \phi / \partial \ln r = -2$ makes negligible difference. At the effective coordinate boundaries where $\cos \theta = \pm 1$, we take $\partial\phi/\partial \cos \theta = \text{const.}$ At the probe, the singularity has already been discussed, but two types of boundary condition on $\partial\phi/\partial\zeta$ have been explored. The simplest, which has been used only for the NGP version of the code, takes $\partial\phi/\partial\zeta = \text{const.}$, which is considered to be the “natural” boundary condition. An alternative, which is used with the CIC version, is to ensure that the normal ion velocity reaches the sound speed at the probe edge. In other words, we apply a Bohm condition. This condition is very prone to particle fluctuations and cannot therefore simply be applied at each step. Instead the difference between the potential at the boundary, which is in the center of the last cell (which therefore is only half populated) and the adjacent radial cell is adjusted smoothly over typically 50 time-steps, via a feedback loop based on the difference between the edge radial speed and the (time-step averaged) sound speed using the local value of the radial ion temperature. The two approaches give consistent results within their uncertainties, as is described later. Attempts to use the “kinetic Bohm condition” [26, 27] showed it to be too subject to noise to be useful.

The SCEPTIC code is written using the Message Passing Interface (MPI) protocols to enable parallel processing for the particle advancing, which is by far the dominant computational cost. The results presented here were obtained with 36 processors of the Beowulf cluster at Alcator, with each processor responsible for typically 200,000 particles, giving a total of 7.2 million particles. The simulation is advanced in time until a steady state is reached. Two to three steps per second (real time) were achieved with 1.2 GHz Athlon processors, and, depending on conditions, roughly 1000 steps were sufficient to reach a steady state.

3 Stationary-plasma solutions and convergence

In view of the subtleties in handling the sheath-edge boundary, and to establish the validity of the SCEPTIC code, it seemed important to benchmark it against previous calculations. A literature search revealed no published quantitative data about particle collection by a sphere in flowing plasmas that could be used for this purpose. However, two references provide detailed quantitative data about the solution to the quasineutral stationary-plasma case with $T_i = T_e$, [6, 9]. [The code cannot be run with zero ion temperature so comparison with the simpler zero-temperature solutions cannot be made.]

For the present purposes, these works provide radial profiles of potential plus the single value of the flux density of ions to the probe. [Parrot et al use a full electron distribution rather than the Boltzmann factor, but their ion flux clearly saturates at moderately negative probe potentials, presumably at the value that would be obtained using the Boltzmann approximation.] Their values of current density, expressed in units of the unperturbed random flux density ($n_\infty(T/2\pi m)^{1/2}$), are 1.47 (Al’pert) and 1.448 (Parrot), which in the present normalization are 0.586 and 0.578 respectively, times $n_\infty(ZT/m)^{1/2}$.

Figure 1 shows an example of the diagnostic output from a stationary-plasma simulation using SCEPTIC. The density is contoured on the plane $z = r \cos \theta$, $r \sin \theta$ in a way that approximates the physical geometry. The spherical configuration is the revolution of this plot about the z -axis. The radial plots of the density show the extreme gradients at the probe edge. They also show excellent spherical symmetry, confirmed also by the angular plots. In all these plots the density is normalized to unity at infinity only roughly, dividing the total particle number by the simulation volume, since the final normalization requires the fitting procedure described previously. All these curves use instantaneous values of the parameters in the simulation, from which the noise level for this case with 100 radial and 30 angular cells, with 7.2M particles may be appreciated. It is quite low for the density except immediately at the sheath edge. Additional dashed curves in the plots versus $\cos \theta$ give 40-step time averages, which naturally show even better spherical symmetry (independence of $\cos \theta$).

The most interesting curves in Fig 1 are perhaps the temperatures. These are defined as the second moment of the distribution function divided by the density, of course, since the distribution is not Maxwellian. The radial temperature drops as the ions are accelerated into the sheath. Tracking this quantity is important because when the sound-speed sheath-edge boundary condition is used, T_r at the edge is required to evaluate the sound speed. By the way, for this purpose the sound speed is evaluated from the expression

$$c_s^2 = \left(\frac{dp_{rr}}{dn} + ZT_e \right) / m, \quad (12)$$

where p is the ion pressure tensor. This expression is more rigorous than simply using the combination $3T_i + ZT_e$, but the results are hardly different. The tangential temperature increases as the probe is approached. This is because of conservation of angular momentum. The temperature is seen to tend to the external value, 1, at the outer boundary, but does not reach it there, because the boundary is fairly close in this case $r_{\max} = 3$.

In figure 2 we show a comparison of the solutions obtained with SCEPTIC and those of Al’pert and Parrot. The agreement is excellent. However, the solution of Parrot has

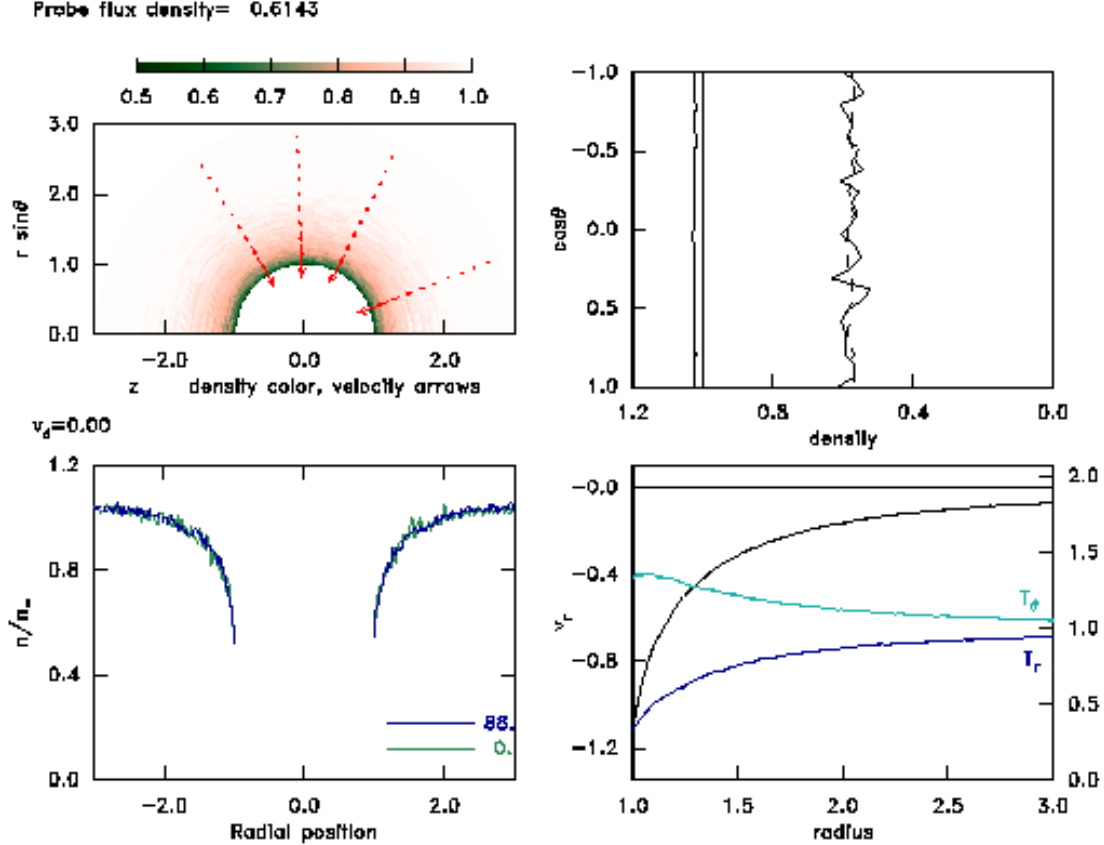


Figure 1: Diagnostics from a stationary-plasma simulation, $T_i = T_e$. Top left, colour contours of plasma density and velocity vectors. Bottom left, radial density variation at angles $\theta = 0, 180^\circ$ and $\theta = 92, 88^\circ$. Top right, density variation with $\cos\theta$ at the probe (dashed line averaged over 40 steps) and averaged over the outer half of the radial domain. Bottom right, velocity and radial and angular ion temperature as a function of radius, averaged over 40 time-steps..

obviously inadequate resolution at the singular probe edge, while Al’pert et al clearly went to considerable effort to resolve it with fine spacing. The SCEPTIC runs shown used 400 radial mesh-points covering the range $1 < r < 3$, thus giving reasonable resolution of the sheath edge. It was found that the outer boundary condition had negligible effect even with this rather modest maximum radius. Ten angular ($\cos\theta$) cells were used here, and of course the solution was independent of angle, so the angle-averaged result is plotted. Moreover, to reduce further the numerical noise level, the results were averaged over the last 40 steps of the simulation, during which it was already converged. The results with the CIC and NGP versions of the code are hardly distinguishable except in the expanded view immediately adjacent to the probe edge, where the natural boundary condition of the NGP version leads to slightly less negative potentials.

If the effect of inaccuracies in the probe boundary condition is mainly to cause an effective

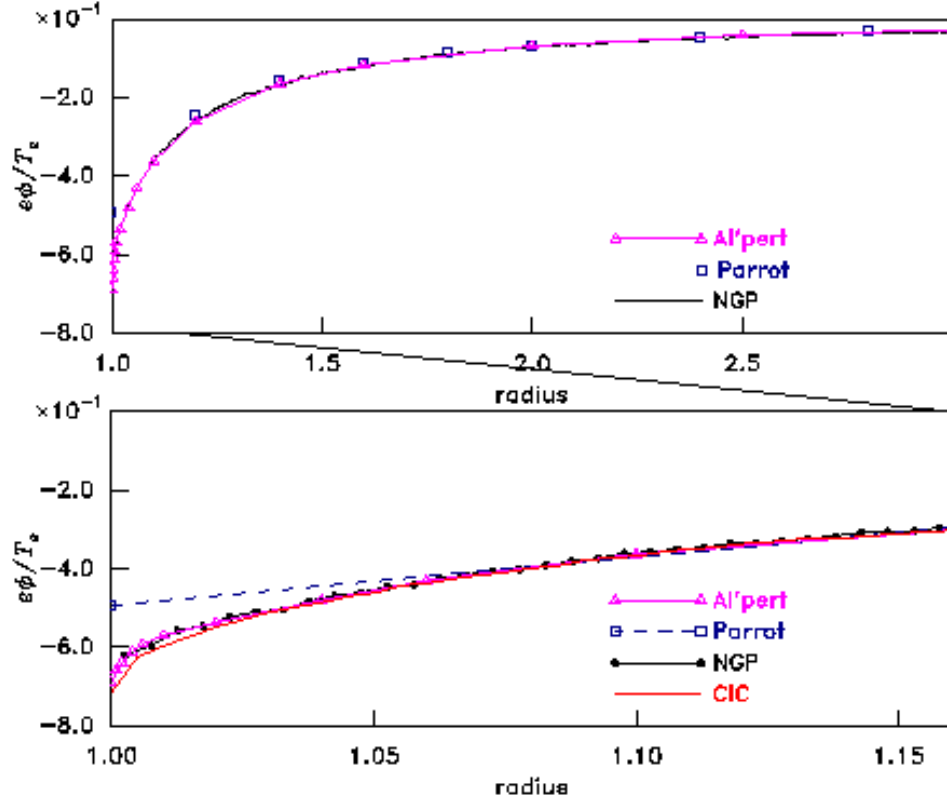


Figure 2: Comparison with prior published results, of the normalized potential versus radius for $T_i = T_e$ as obtained from the two versions of the SCEPTIC code (NGP and CIC). The lower plot is an expansion of the edge region.

sheath edge at a radial position slightly different from $r = 1$, then, by inspection of this plot, the resulting uncertainty is no more than approximately 0.003 (times the probe radius), which would correspond to a fractional area uncertainty of 0.006 (0.6%). The differences between the PIC values of normalized potential are less than 0.005 everywhere except in the last two cells. The agreement of the PIC results is better than the Parrot results with those of Al'pert. In short, highly satisfactory agreement is obtained in the potential profile.

The same cannot be said for the value of the ion flux to the probe. Therefore a detailed convergence study of the code was undertaken, to determine the dependence of the flux on the number of radial mesh points, and thus the resolution. The flux is determined by counting the particles that hit the probe at each step. The normalized flux density is then the average per step, divided by the area, divided by the step time, and divided by the normalization factor needed to scale the density to make $n_{i\infty} = 1$. Some care must be taken to ensure that as the mesh spacing is varied the timestep is adjusted to avoid numerical instabilities. For this reason, more steps are needed for the finer mesh spacings. Some illustrative results are shown in Fig 3, along with the published values of Al'pert et al and of Parrot et al.

The most striking fact is that there is serious disagreement of the results of the SCEPTIC

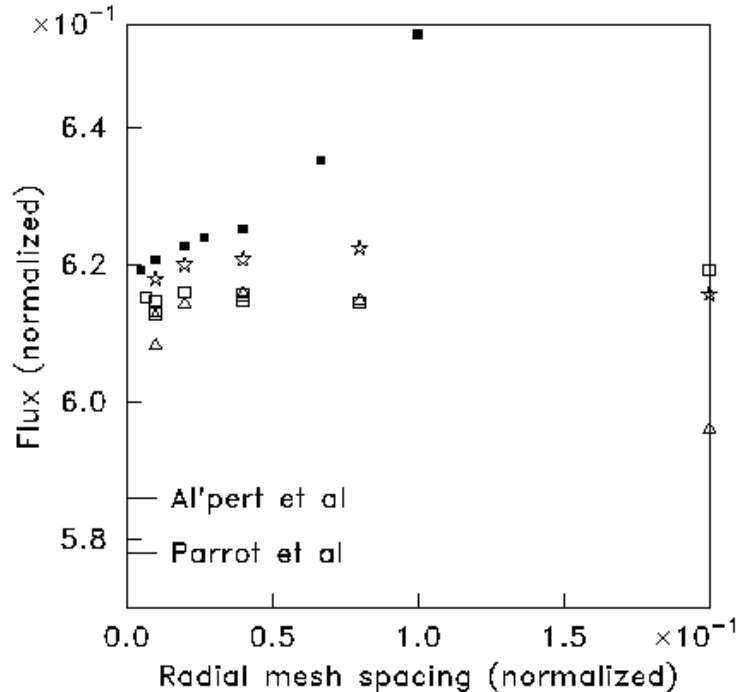


Figure 3: Dependence of the average normalized ion flux density on mesh spacing obtained with different sized radial mesh, for different versions of the SCEPTIC code. (Open squares: production CIC; triangles: production NGP; stars: Bohm-condition NGP; filled squares: linear interpolation NGP.)

code with the published values. The two production versions of the code use the square-root scaling approach described in section 2.2. They agree with each other within about 1% for mesh spacing up to 0.08, but at greater spacing (0.2) the natural boundary condition of the NGP code gives rather lower flux. This extreme spacing would correspond to only 10 radial mesh points in $1 < r < 3$. A version of the NGP code with the enforcement of sound-speed flow at the boundary (i.e. the Bohm condition, similar to the CIC code) gives somewhat (about 1%) higher results but does not show the larger discrepancy with coarse spacing. A version that does not use the square-root scaling at the sheath edge shows much larger discrepancies but seems to converge (slowly) to the same flux for very fine spacing. The results of the production SCEPTIC code converge to a value that may be taken conservatively as 0.614 ± 0.006 . This is significantly higher, by about 6%, than the values given by Parrot and Al'pert, which themselves differ by about 2%. It is unknown what the source of this difference is. One speculation is that it might arise from dynamics far from the probe, for example some effective collision length relative to angular momentum conservation. Simulations give a flux value that appears independent of r_{\max} , which tends to discount this suggestion. Another possibility is that the effective treatment of trapped orbit particles might be different. Normally it is presumed that trapped orbits are not quantitatively important. It might be, however, simply that the flux integrations in the

prior works were relatively inaccurate. It is hard to see how the results can be so inaccurate in a PIC code, since particles are perfectly conserved.

In subsequent sections, we use lower radial mesh resolution, corresponding to a spacing of typically 0.04. Judging by Fig 3, the results are well converged at such a spacing.

4 Flowing Plasma Results

The primary results of the present work are the ion current density to the probe, resolved in angle, and its dependence on the flow velocity and ion temperature.

Fig 4 shows the normalized ion flux as a function of $\cos\theta$ for a range of flow velocities (marked on the curves) and $T_i = 1$ (times T_e). The CIC scheme is used here. The radial and angular meshes used are 100×30 , and $r_{\max} = 5$ is sufficient to give flux values little affected by the outer boundary.

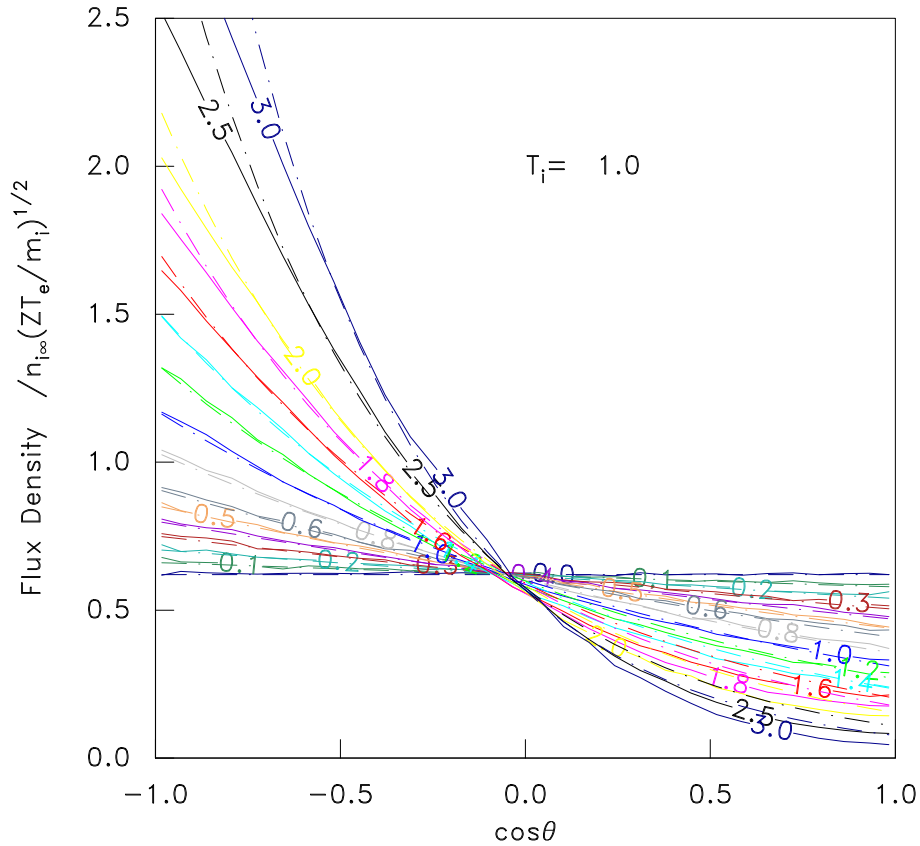


Figure 4: Ion flux density to the sphere, normalized to $n_{i\infty}(ZT_e/m)^{1/2}$, as a function of $\cos\theta$ for $T_i = T_e$. The SCEPTIC results are solid lines; the fit of eq (13) is indicated by chain curves.

A plot like this provides the fundamental data that is derived from the simulations. However, it is helpful also to have a compact representation of the data in approximate analytic form. It is clear by inspection, and also by perturbation analysis, that the angular

variation of the flux density $\Gamma(v_f, \cos \theta)$ at small flow velocities, can be approximated to first order by a straight line: $\Gamma(v_f, \cos \theta) - \Gamma(0, 0) \propto v_f \cos \theta$. This is naturally the first asymmetric spherical harmonic. Plainly, that approximation breaks down as v_f approaches 1, and the curves must become concave. It transpires that a reasonable universal fit to all the curves is obtained with the 3-parameter form

$$\Gamma(v_f, \cos \theta) = \Gamma_0 \exp\{v_f[(1 - \cos \theta)K_u - (1 + \cos \theta)K_d]/2\}, \quad (13)$$

with $\Gamma_0 = 0.62$, $K_u = 0.64$, and $K_d = 0.70$. The fit is illustrated in Fig 4. It agrees with the numerical results within their uncertainty for $v_f \leq 1.2$. At higher flow velocities the fit is increasingly inadequate, especially on the downstream side ($\cos \theta > 0$), but for purposes of Langmuir probe interpretation, where experimental uncertainties up to 30% are not unusual, the fit is certainly useful to at least $v_f = 2.5$.

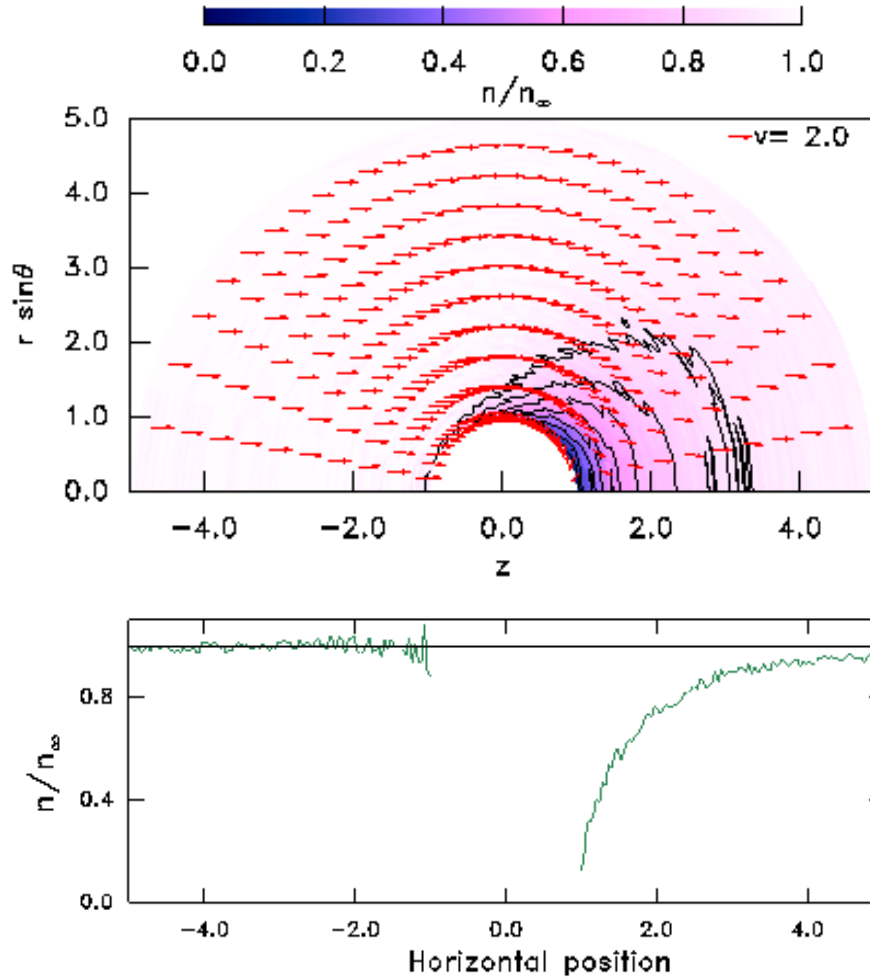


Figure 5: Contour plot of the density near a probe with $T_i = T_e$ and $v_f = 2$. Mean (fluid) velocity at a subset of the cells is shown by vector arrows. The lower figure shows the density along the axis of symmetry.

In Fig 5 are shown examples of plasma parameters for a flow velocity $v_f = 2$. This speed equals the (adiabatic) sound speed in the unperturbed plasma, although there is nothing qualitatively unusual about the results for this specific value. The upstream density is hardly perturbed. There is no need for a potential drop to satisfy the Bohm condition, because the flow is already at the sound speed. For higher flow speeds the upstream remains unperturbed. The increase of the noise level close to the probe is visible; it is mostly caused by decreasing cell size. On the downstream side, a deep potential well forms close to the probe. However, as can be seen from the vector plot of (distribution-averaged) velocity, the multidimensional nature of the solution is an essential factor in the problem, and the downstream velocity is diverted to give a sound-speed flow into the probe by the integrated effect of the electric field around the periphery of the probe, not just by direct acceleration in the z -direction. Moreover, the flow divergence in the z -direction immediately downstream from the probe is balanced by the convergence of the azimuthal flow there.

The contours in Fig 6 show that the upstream temperatures are hardly changed from the external value (namely 1). But that on the downstream side, extremely strong anisotropy

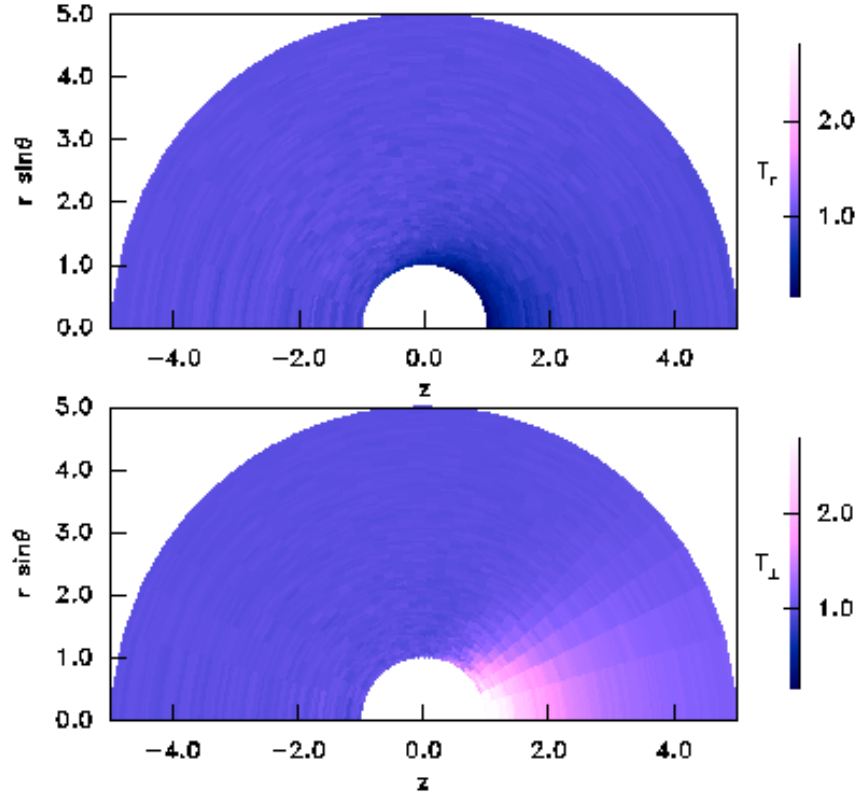


Figure 6: Color contours of radial temperature (top) and tangential temperature (bottom), for the case of Fig 5.

occurs, with cooling by a factor of roughly two of the radial temperature, and heating by even more of the tangential temperature. Of course, especially in the tangential direction, the

distribution function is not at all Maxwellian. Figure 7 shows the distribution functions in the radial and the azimuthal components of velocity, averaged over 500 time steps for the first cell in radius and in $\cos \theta$, that is, closest to the probe on the down-stream side. The units are simply the total number of particle counts in each velocity bin. The radial distribution has,

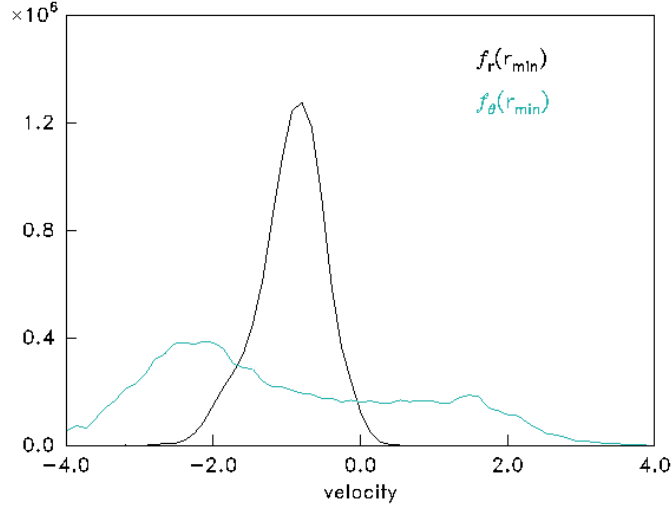


Figure 7: Ion distribution functions in radial and azimuthal velocity, for the case of Fig 5, in the first downstream angular cell, at the sheath-edge.

of course, almost all negative-going particles. The asymmetry in the azimuthal distribution arises because the cell is not on axis, but extends in angle from zero to approximately 20° . The two-humped form arises from particles accelerated around the probe from opposite sides.

The SCEPTIC code works without difficulty for $T_i/ZT_e \gtrsim 1$ both at subsonic and supersonic flow velocities. However, as the ion temperature is reduced substantially below the electron temperature the code eventually becomes subject to a numerical instability called the finite-grid instability. This instability is commonplace in electron PIC codes[24, 25], but also is experienced by hybrid codes[28] like SCEPTIC. The unstable waves in this case are sound waves, whose ion Landau damping becomes rapidly smaller as T_i/ZT_e is reduced. It manifests itself as non-physical heating of the ions caused by enhanced fluctuations, and is experienced with the NGP version for $T_i/ZT_e \lesssim 0.2$. Consistent with the observations of Rambo[28] the CIC code is less susceptible to this problem and no numerical heating is observed on SCEPTIC down to $T_i/ZT_e = 0.1$.

Fig 8 shows the normalized ion flux as a function of $\cos \theta$ for a range of flow velocities (marked on each curve). Each plot is for a chosen ion temperature (normalized to ZT_e) in the range $0.1 \leq T_i \leq 10$. The CIC code is used for $T_i/ZT_e \leq 1$. and the NGP code for other values, although the CIC code gives the same result within uncertainties. We take $T_i/ZT_e = 0.1$ as the lower limit of the present study, and do not explore beyond $T_i/ZT_e = 10$ because results indicate that the approximation of ignoring the self-consistent field is quite good for that ion temperature and above. (The numerical data is given in the appendix.)

To summarize the content of these calculations, Fig 9 shows the flux density at the axis of

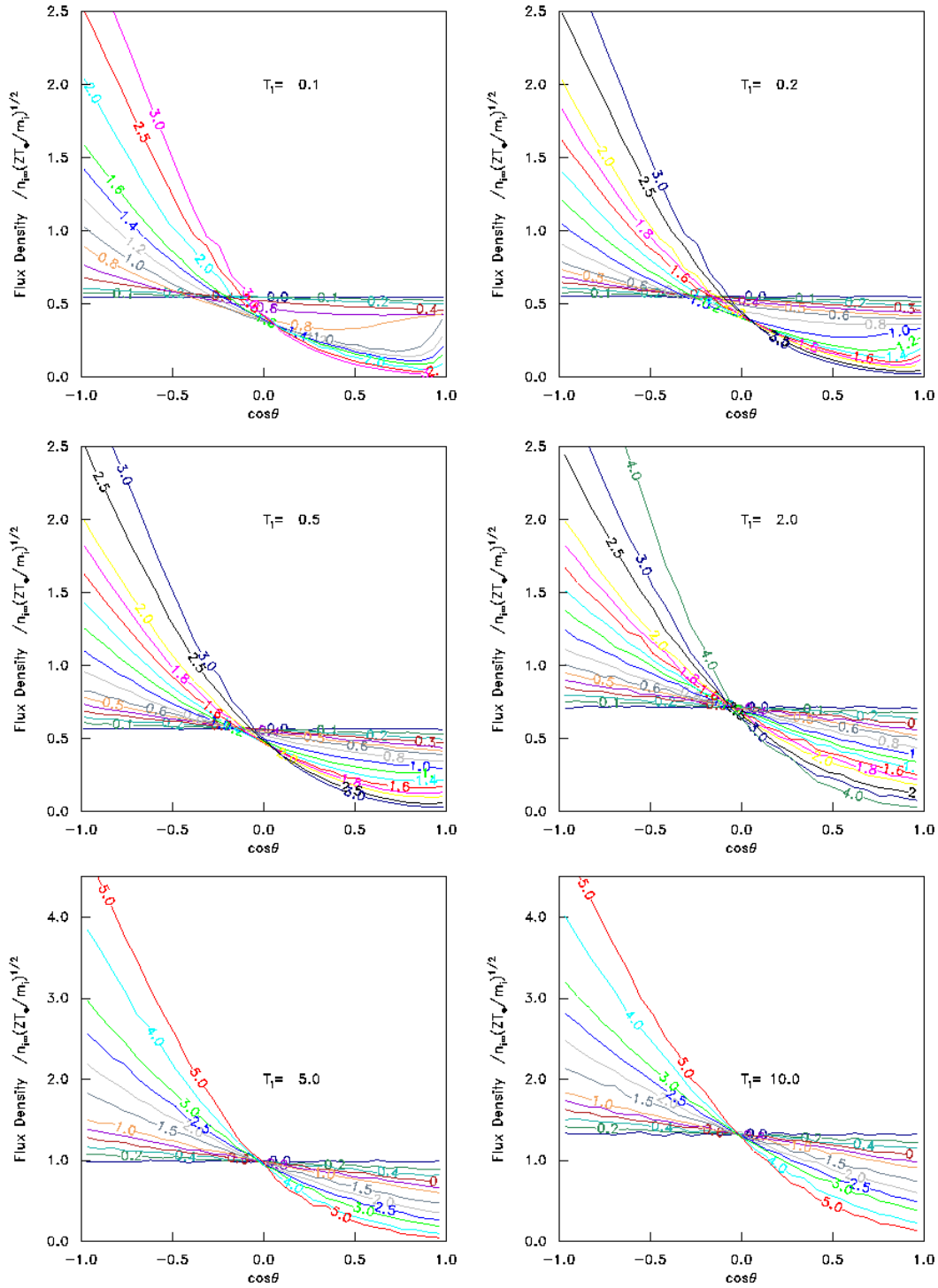


Figure 8: Ion flux density normalized to $n_{i\infty}(ZT_e/m)^{1/2}$, as a function of $\cos\theta$ for different flow velocities, as indicated on the curves, and a range of ion temperatures.

symmetry ($|\cos \theta| = 1$) upstream and downstream as a function of drift velocity. Additional $T_i = 1$ data from runs using the CIC version (as per Fig 6), and the NGP versions with natural, and Bohm, sheath conditions are included. It can be seen that they agree within a few percent which is roughly our uncertainty.

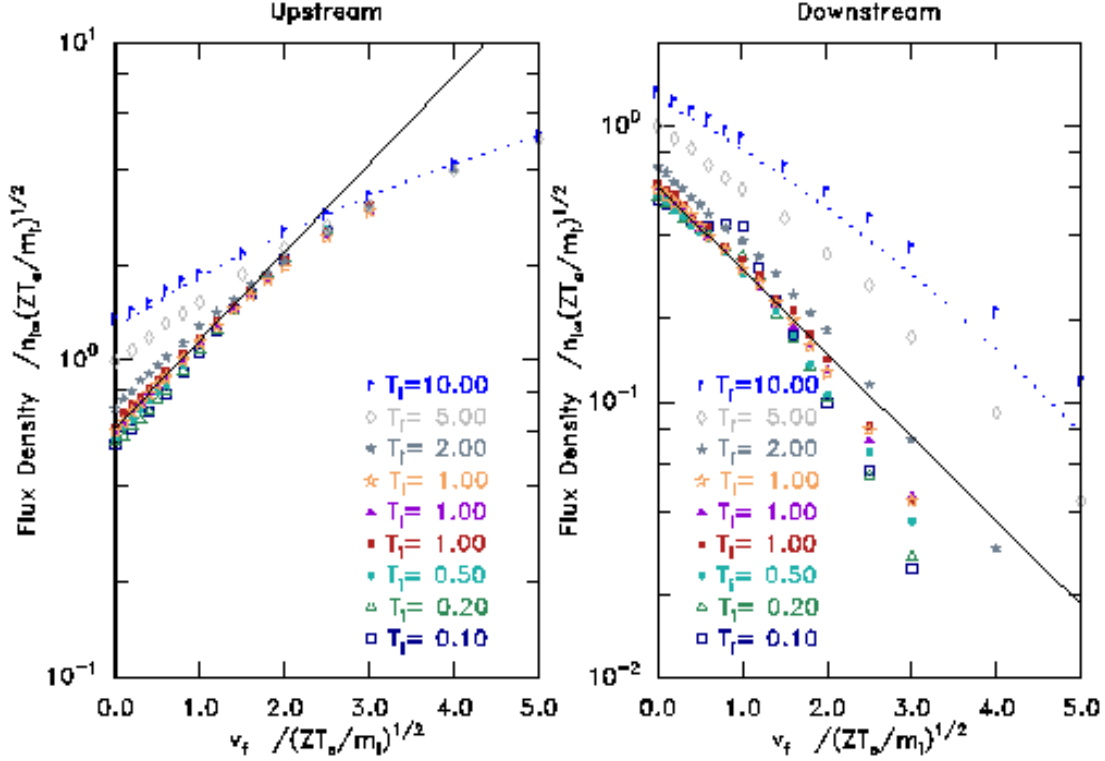


Figure 9: Flux density to the probe at $|\cos \theta| = 1$ (the axis of symmetry) upstream and downstream, for the range of temperatures as a function of flow velocity. The solid line is the fit, eq (13). The dotted line is the result of neglecting electric field, for $T_i = 10$, giving the analytical result eq (10).

With some notable exceptions at low T_i , the results are quite close to the fit of eq(13) noted for unity ion temperature. The slope of the curves at low velocity is remarkably similar to the line of fit. There is modest variation in the absolute flux about the line, and at high velocities and low temperatures, the points fall lower on the downstream side.

At high temperatures the results deviate more strongly from the fit, and by $T_i = 10$, the analytic “free-flight” result eq (10), obtained by neglecting the electric field, begins to fit the data quite well. Naturally, in the limit $T_i \gg 1$, that approximation is expected to become accurate, when thermal ion energies far exceed the typical potential energy, $ZT_e = 1$.

The ratio of upstream to downstream ion current is shown in Fig 10. This is the quantity determining the calibration factor of a Mach probe. The results for different temperatures

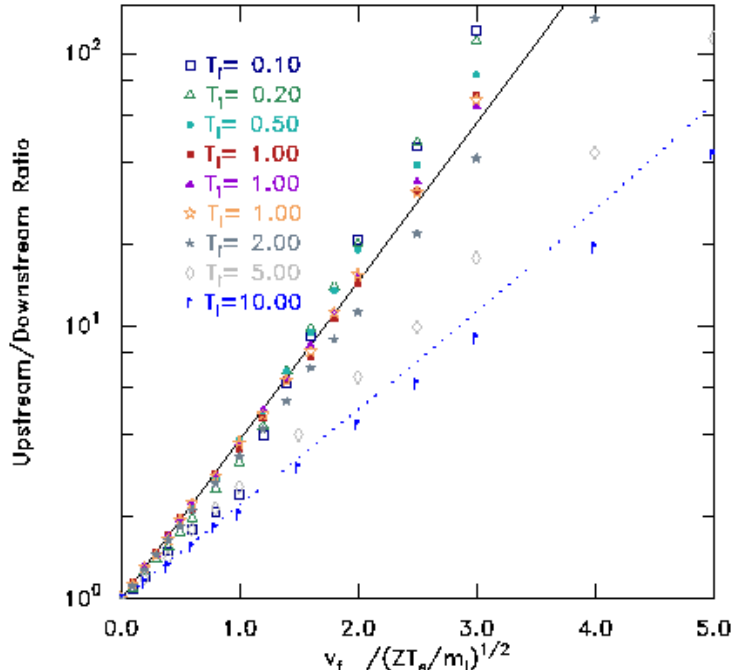


Figure 10: Ratio of current density upstream to downstream for the same data as Fig 9.

are even closer together for $T_i < 5$, and close to the line obtained from eq (13), namely

$$\frac{\Gamma_{\text{up}}}{\Gamma_{\text{down}}} = \exp(Kv_f), \quad (14)$$

with $K = K_u + K_d = 1.34$. At $T_i \geq 10$ the analytic free-flight expression is quite a good fit, and the flow velocity for a specific ratio becomes proportional to $\sqrt{T_i}$.

At low temperature there are substantial deviations from the line of fit for velocities of order unity or just below. This effect is particularly noticeable for $T_i = 0.1$. It consists of the downstream flux density being higher than the trend. Inspection of Fig 8 show that the cause is that the flux density is non-monotonic in $\cos\theta$, there being a secondary peak on the downstream axis. Physically this arises because of focusing of the ions onto the axis on the downstream side, which has sufficient effect even at small radii to raise the probe flux. When the flow velocity is high enough, the effect at the probe disappears, although it does not disappear in the wake. Fig 11 shows density contours illustrating the wake, obtained for a higher resolution (100×100) mesh at low ion temperature. Experiments [29, 30] and prior theory[12, 14] and simulations [13] have previously documented this effect in the wake structure. With ion temperature low enough to prevent dominant Landau damping, a rarefaction cone appears, whose angle at high velocity is approximately given by the usual Čerenkov condition, and a density peak on axis. Simulation of the wake region was not the major purpose of this study or the SCEPTIC code, but it is gratifying to see it reproduce one of the major results of a topic that has received considerable attention.

Since the effect is localized to the axis, and is dependent on the spherical geometry, its

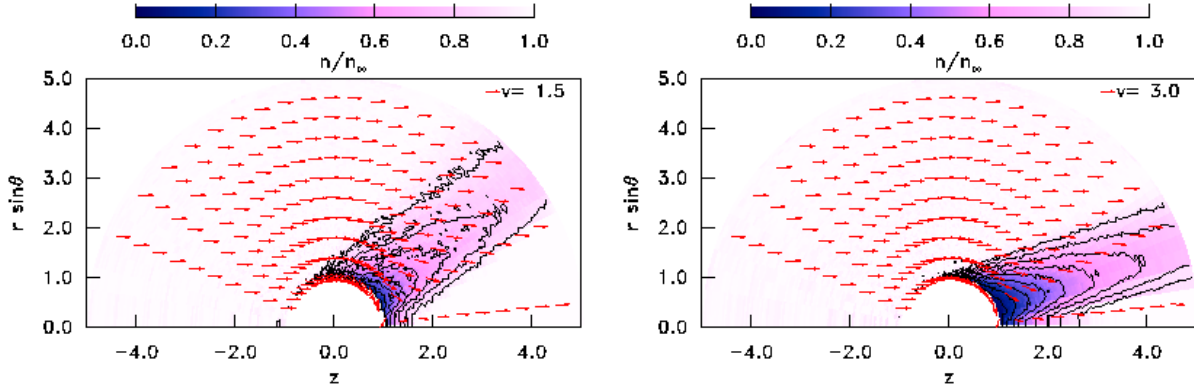


Figure 11: Density contours and velocity vectors in a plasma with low ion temperature ($T_i = 0.1ZT_e$) and flow 1.5, and 3.0 times the sound speed.

effect on Mach probe calibration seems likely to be less severe in practice than might be thought from the data of Fig 10.

5 Discussion

With the exception of the free-flight analytic solution, valid at high T_i/ZT_e , no rigorous prior theoretical calculations of the unmagnetized Mach probe calibration appear to exist. However, experiments have been performed, and some of them had independent information about flow. The difficulty with quantitative comparisons is that essentially none of the experiments used a probe geometry even remotely approximating the idealized sphere that has been analysed here. Since the ion dynamics plainly depends on the multidimensional geometry, there is no a priori reason to believe that the calibration is independent of the shape of the probe, and indeed it may not be. Further simulations need to be done to investigate this question.

Nevertheless, it is interesting to compare the calibration factor obtained here with what has been previously proposed or used on an empirical or theoretical basis. The whole question can be boiled down to providing the value of the calibration coefficient K in eq (14). In all cases the exponential form is a rather good approximation, but even if it weren't we could regard the coefficient as giving the logarithmic gradient at the origin, which is the calibration for slow flow.

In Table 1 are given the calibration factors from different sources. The fit to present results is simply a constant, $K = 1.34$ accurate to 10% or better, for $T_i \lesssim 3$ (times ZT_e). Figure 10 gives a more complete assessment of the accuracy. At high $T_i \gtrsim 10$ the free-flight eq (10) applies.

The heuristic formula of Hudis and Lidsky, like some other fluid theories, is somewhat ambiguous since it refers to a sound-speed c_s to be applied at the sheath edge. The ion temperature there is substantially less than at infinity, so it is unclear what value to use in c_s . Here, for simplicity, we take the sound speed to be given by the isothermal formula

Table 1: Comparison of Mach Probe calibration factors

Author	K formula	$K(T_i = 1)$	Description	Ref
Present work	1.34 for $T_i \lesssim 3$	1.34	fit to SCEPTIC	
Eq 10	$\sqrt{2\pi T_e/T_i}$	2.5	Free-flight	[6]
Hudis & Lidsky	$4(T_i T_e)^{1/2}/(T_e + T_i)$	2	Heuristic	[18]
Schats et al	$4\sqrt{T_e/T_i}$	4	Heuristic	[19]
Solomon & Schats	$(4/\pi)\sqrt{T_i/T_e}$	1.27	Heuristic	[20]
Chung et al	1.26 @ $T_i = 0.1$		Experiment	[31]
Oksuz et al	1.3 @ $T_i = 0.1$		Experiment	[32]
Hutchinson	$(0.43\sqrt{1 + T_i/T_e})^{-1}$	1.64	Magnetized, fluid	[15]
Chung & Hutchinson		1.7	Magnetized, kinetic	[16]

$c_s = [(T_e + T_i)/m]^{1/2}$ (taking $Z = 1$ to avoid cumbersome notation). We substitute the unperturbed T_i in this formula. The error of ignoring the factor of 3 (ratio of specific heats for one degree of freedom adiabatic ions) roughly cancels the error of ignoring the temperature variation. Some comparisons of magnetized Mach probe fluid theories indicate this approach is an acceptable approximation[33] in that context.

The unsatisfactory nature of heuristic arguments is illustrated by the fact that the different formulas of Schats et al, and of Solomon and Schats both claim to be extensions of the arguments of Hudis and Lidsky, but are quantitatively and qualitatively very different. In the absence of rigorous calculations, the choice of such theories is a matter of unjustified “taste”. None can be regarded as properly justified.

The experiments of Chung et al [31] are based on comparing magnetized with unmagnetized Mach probes in the same plasma. They found reasonable consistency between the two using $K = 1.26$ for the unmagnetized probes, when $T_i = 0.1T_e$. (But the magnetized probes were subject to the effects of connection of the presheath along the field to the end plates[34].) Oksuz et al [32] measured the ion velocity using laser induced fluorescence. They found good agreement when using the Hudis and Lidsky formula at $T_i = 0.1T_e$, which is $K \approx 1.3$. It is encouraging that the two experimental values, confirmed by independent velocity measurements, agree with the present work within their uncertainty. It may indicate that the value obtained here has validity wider than just to spherical probes. However, confirmation over more of the temperature range is surely needed.

The final two values are the accepted theories for magnetized Mach probes. The kinetic calculations agree rather well with the fluid calculations, but shear viscosity can affect the result. The cited values take viscous momentum diffusivity to equal particle diffusivity. It should be noted that the values of K are significantly greater for these magnetized cases than the present unmagnetized values.

6 Conclusions

The ion flux to a spherical body in a collisionless plasma with negligible Debye length, has been calculated for a wide range of temperatures and flow speeds. In addition to the numerical data, compact analytic approximations fitting the data have been given, equations (13) and (14). These provide a rigorous theoretical calibration of unmagnetized Mach probes, at least for this particular geometry. Although the agreement with the plasma potential profile of prior quasineutral calculations in stationary plasmas is excellent, a theoretically significant discrepancy has been found in the ion flux to the probe. The value obtained here, whose uncertainty is estimated to be approximately 1%, is 6% higher than prior published values. In rapidly flowing plasmas at low ion temperature, wake structure and associated ion focussing affect the ion collection, causing flux density to be a non-monotonic function of angle.

7 Acknowledgements

I am grateful to Howard Yuh for implementing the Alcator Beowulf cluster, which is supported by DOE grant DE-FC02-99ER54512, and for many helpful discussions on parallel processing. I benefitted also from discussions on PIC code techniques with Edmund Bertschinger.

References

- [1] H. M. Mott-Smith and I. Langmuir. *Phys. Rev.*, 28:727, 1926.
- [2] L. Tonks and I. Langmuir. *Phys. Rev.*, 34:876, 1929.
- [3] D. Bohm. In A. Guthrie and R. K. Wakerling, editors, *Characteristics of Electrical Discharges in Magnetic Fields*. McGraw-Hill, New York, 1949.
- [4] J. E. Allen, R. L. F. Boyd, and P. Reynolds. *Proc. Phys. Soc*, 70B:297, 1957.
- [5] I. B. Bernstein and I. Rabinowitz. *Phys. Fluids*, 2:112, 1959.
- [6] Ya. L. Al’pert, A. V. Gurevich, and L. P. Pitaevskii. *Space Physics with Artificial Satellites*. Consultants Bureau, New York, 1965.
- [7] J. Laframboise. In J. H. deLeeuw, editor, *Rarified Gas Dynamics*, , Vol. 2, p. 22. New York, 1966. Academic. (Also Univ. of Toronto Institute for Aerospace Studies Report No. 100.). Proc. 4th Int. Symp., Toronto.
- [8] J. Virmont and R. Godard. *Plasma Phys.*, 14:793, 1972.
- [9] M. J. M. Parrot, L. R. O. Storey, L. W. Parker, and J. G. Laframboise. *Phys. Fluids*, 25:2388, 1982.

- [10] F. F. Chen. *Plasma Phys.*, 7:47, 1965.
- [11] A. V. Gurevich, L. P. Pitaevskii, and V. V. Smirnova. *Space Sci. Rev.*, 9:805, 1969.
- [12] N. I. Budko. *Soviet Physics JETP*, 30:375, 1970.
- [13] E. Coggiola and A. Soubeyran. *J. Geophys. Res.*, 96:7613, 1991.
- [14] M. A. Morgan, C. Chan, Cooke D. L., et al. *IEEE Trans Plasma Sci*, 17:220, 1989.
- [15] I. H. Hutchinson. *Phys. Rev. A*, 37:4358, 1988.
- [16] K.-S. Chung and I. H. Hutchinson. *Phys. Rev. A*, 38:4721, 1988.
- [17] J.P. Gunn, C. Boucher, P. Devynck, I. Duran, K. Dyabilin, J. Horacek, M. Hron, J. Stokel, G. Van Oost, H. Van Goubergen, and F. Zacek. *Phys. Plasmas*, 8:1995, 2001.
- [18] M. Hudis and L. M. Lidsky. *J. Appl. Phys.*, 41:5001, 1970.
- [19] M. G. Schats, Rudakov D. L., R. W. Boswell, et al. *Phys. Plasmas*, 4:3629, 1997.
- [20] W. M. Solomon and Schats M. G. *Rev. Sci. Instrum.*, 72:449, 2001.
- [21] S. Shinohara, N. Matsuoka, and S. Matsuyama. *Phys. Plasmas*, 8:1154, 2001.
- [22] S. C. Hsu, F. A. Carter, G. Fiksel, et al. *Phys. Plasmas*, 8:1916, 2001.
- [23] I. H. Hutchinson. *Phys. Plasmas*, 9:1832, 2002.
- [24] R. W. Hockney and J. W. Eastwood. *Computer Simulation Using Particles*. IOP Publishing, Bristol, 1988.
- [25] C. K. Birdsall and A. B. Langdon. *Plasma Physics via Computer Simulation*. IOP Publishing, Bristol, 1991.
- [26] E. R. Harrison and W. B. Thompson. *Proc. Phys. Soc*, 74:145, 1959.
- [27] K.-U. Reimann. *J. Phys. D*, 24:493, 1991.
- [28] P. W. Rambo. *J. Comp. Phys.*, 118:152, 1995.
- [29] N. H. Stone. *J. Plasma Phys.*, 25:351, 1981.
- [30] R. L. Merlino and N. D'Angelo. *J. Plasma Phys.*, 37:185, 1987.
- [31] K. S. Chung, I. H. Hutchinson, B. LaBombard, and R. W. Conn. *Phys. Fluids B*, 1:2229, 1989.
- [32] L Oksuz, M. A. Khedr, and N. Hershlowitz. *Phys. Plasmas*, 8:1729, 2001.
- [33] M. Laux, H. Grote, K. Guenther, A. Herrmann, D. Hildebrandt, P. Pech, Reiner H.-D., H. Wolff, and G. Ziegenhagen. *J. Nucl. Mater.*, 162-164:200, 1989.
- [34] I. H. Hutchinson. *Phys. Fluids B*, 3:847, 1991.

A Data tables

Here we present in tabular form, for reference, most of the data in figure 8.

Table 2: Dependence of ion flux to the sphere on flow velocity and angle when $T_i = 0.1ZT_e$.

$v_f:$ $\cos \theta$	0.000	0.100	0.200	0.400	0.600	0.800	1.000	1.200	1.600	2.000	2.500	3.000
	Ion Flux density, Γ ($/n_{i\infty}(ZT_e/m)^{1/2}$)											
-0.983	0.546	0.575	0.606	0.684	0.769	0.896	1.030	1.218	1.590	2.044	2.509	2.990
-0.931	0.547	0.576	0.606	0.668	0.740	0.848	0.976	1.153	1.505	1.936	2.378	2.831
-0.862	0.546	0.575	0.599	0.654	0.709	0.801	0.913	1.072	1.393	1.770	2.187	2.631
-0.793	0.547	0.572	0.593	0.640	0.686	0.757	0.852	0.996	1.286	1.620	2.015	2.414
-0.724	0.546	0.569	0.587	0.628	0.658	0.718	0.799	0.917	1.171	1.480	1.820	2.208
-0.655	0.550	0.569	0.584	0.615	0.636	0.677	0.747	0.857	1.071	1.321	1.641	1.980
-0.586	0.546	0.564	0.581	0.603	0.608	0.645	0.704	0.790	0.974	1.188	1.462	1.769
-0.517	0.549	0.562	0.576	0.589	0.591	0.606	0.650	0.736	0.881	1.051	1.296	1.558
-0.448	0.548	0.563	0.569	0.581	0.573	0.574	0.609	0.675	0.807	0.963	1.119	1.345
-0.379	0.551	0.553	0.568	0.568	0.552	0.540	0.569	0.625	0.714	0.867	0.970	1.139
-0.310	0.549	0.555	0.561	0.563	0.534	0.512	0.527	0.575	0.648	0.741	0.900	0.963
-0.241	0.550	0.555	0.558	0.546	0.520	0.486	0.493	0.527	0.583	0.685	0.740	0.898
-0.172	0.548	0.556	0.554	0.544	0.506	0.460	0.459	0.485	0.534	0.554	0.646	0.694
-0.103	0.551	0.554	0.550	0.531	0.492	0.433	0.422	0.445	0.465	0.538	0.535	0.610
-0.034	0.548	0.549	0.552	0.527	0.476	0.411	0.396	0.405	0.419	0.425	0.452	0.457
0.034	0.547	0.552	0.542	0.520	0.471	0.392	0.366	0.371	0.376	0.400	0.386	0.399
0.103	0.548	0.550	0.544	0.508	0.460	0.375	0.340	0.337	0.332	0.327	0.322	0.306
0.172	0.546	0.543	0.534	0.506	0.448	0.351	0.311	0.307	0.292	0.295	0.275	0.256
0.241	0.548	0.543	0.532	0.495	0.445	0.343	0.289	0.276	0.265	0.256	0.228	0.206
0.310	0.546	0.545	0.532	0.497	0.439	0.332	0.269	0.254	0.228	0.206	0.185	0.169
0.379	0.548	0.543	0.525	0.491	0.433	0.325	0.250	0.228	0.205	0.195	0.158	0.136
0.448	0.548	0.538	0.520	0.484	0.433	0.331	0.227	0.210	0.180	0.154	0.132	0.107
0.517	0.548	0.537	0.518	0.480	0.430	0.335	0.221	0.187	0.156	0.133	0.104	0.084
0.586	0.551	0.533	0.519	0.479	0.431	0.347	0.194	0.176	0.137	0.115	0.089	0.067
0.655	0.552	0.531	0.513	0.475	0.424	0.371	0.193	0.156	0.116	0.097	0.072	0.053
0.724	0.549	0.527	0.511	0.471	0.430	0.385	0.175	0.149	0.103	0.076	0.058	0.041
0.793	0.551	0.531	0.508	0.469	0.431	0.401	0.186	0.142	0.091	0.074	0.046	0.029
0.862	0.550	0.530	0.504	0.464	0.432	0.415	0.210	0.150	0.089	0.054	0.037	0.024
0.931	0.549	0.526	0.503	0.461	0.431	0.424	0.299	0.194	0.101	0.063	0.031	0.018
0.983	0.545	0.524	0.502	0.460	0.432	0.435	0.400	0.280	0.156	0.091	0.050	0.023

Table 3: Dependence of ion flux to the sphere on flow velocity and angle when $T_i = 0.2ZT_e$.

$v_f:$ $\cos \theta$	0.000	0.100	0.200	0.400	0.600	0.800	1.000	1.200	1.600	2.000	2.500	3.000
	Ion Flux density, Γ ($/n_{i\infty}(ZT_e/m)^{1/2}$)											
-0.983	0.552	0.575	0.616	0.685	0.790	0.910	1.052	1.214	1.621	2.038	2.494	3.013
-0.931	0.552	0.583	0.605	0.680	0.762	0.876	0.998	1.150	1.530	1.910	2.367	2.855
-0.862	0.554	0.580	0.606	0.659	0.736	0.828	0.937	1.075	1.425	1.758	2.177	2.619
-0.793	0.552	0.568	0.596	0.647	0.706	0.793	0.884	0.995	1.307	1.610	2.003	2.418
-0.724	0.552	0.574	0.590	0.632	0.684	0.748	0.822	0.925	1.194	1.474	1.832	2.192
-0.655	0.552	0.569	0.586	0.620	0.659	0.709	0.772	0.860	1.093	1.335	1.635	1.990
-0.586	0.555	0.570	0.580	0.605	0.636	0.676	0.721	0.796	0.994	1.190	1.480	1.763
-0.517	0.552	0.566	0.577	0.597	0.619	0.646	0.681	0.735	0.899	1.068	1.297	1.555
-0.448	0.554	0.561	0.569	0.589	0.596	0.608	0.638	0.691	0.837	0.951	1.140	1.349
-0.379	0.549	0.557	0.570	0.575	0.575	0.587	0.595	0.634	0.745	0.885	0.994	1.153
-0.310	0.550	0.559	0.563	0.564	0.564	0.554	0.553	0.584	0.682	0.745	0.897	0.981
-0.241	0.553	0.555	0.558	0.551	0.540	0.533	0.518	0.540	0.606	0.696	0.761	0.913
-0.172	0.551	0.552	0.547	0.548	0.534	0.505	0.490	0.498	0.561	0.578	0.659	0.713
-0.103	0.551	0.552	0.552	0.535	0.513	0.480	0.454	0.456	0.487	0.542	0.554	0.618
-0.034	0.552	0.550	0.540	0.526	0.501	0.463	0.426	0.420	0.451	0.453	0.476	0.488
0.034	0.554	0.547	0.539	0.520	0.488	0.443	0.401	0.389	0.394	0.407	0.404	0.414
0.103	0.550	0.545	0.535	0.510	0.472	0.434	0.373	0.355	0.358	0.348	0.338	0.335
0.172	0.548	0.542	0.531	0.502	0.468	0.409	0.353	0.325	0.316	0.301	0.285	0.273
0.241	0.551	0.543	0.527	0.496	0.456	0.398	0.329	0.303	0.277	0.268	0.241	0.224
0.310	0.556	0.539	0.522	0.488	0.446	0.392	0.311	0.274	0.250	0.226	0.203	0.175
0.379	0.552	0.537	0.517	0.484	0.436	0.379	0.299	0.254	0.217	0.194	0.166	0.145
0.448	0.552	0.534	0.516	0.478	0.431	0.375	0.285	0.231	0.195	0.171	0.138	0.115
0.517	0.552	0.534	0.512	0.472	0.425	0.367	0.274	0.214	0.171	0.143	0.113	0.093
0.586	0.549	0.527	0.509	0.467	0.422	0.363	0.276	0.202	0.150	0.122	0.093	0.072
0.655	0.554	0.531	0.506	0.459	0.411	0.360	0.275	0.187	0.136	0.103	0.075	0.055
0.724	0.553	0.528	0.506	0.455	0.410	0.359	0.283	0.181	0.119	0.090	0.060	0.044
0.793	0.553	0.527	0.499	0.451	0.411	0.359	0.299	0.188	0.109	0.074	0.051	0.034
0.862	0.554	0.523	0.499	0.451	0.402	0.362	0.310	0.201	0.105	0.067	0.041	0.025
0.931	0.549	0.522	0.490	0.442	0.399	0.366	0.325	0.238	0.123	0.071	0.039	0.023
0.983	0.550	0.520	0.491	0.444	0.403	0.363	0.335	0.274	0.157	0.095	0.050	0.026

Table 4: Dependence of ion flux to the sphere on flow velocity and angle when $T_i = 0.5ZT_e$.

v_f : $\cos \theta$	0.000	0.100	0.200	0.400	0.600	0.800	1.000	1.200	1.600	2.000	2.500	3.000
	Ion Flux density, Γ ($/n_{i\infty}(ZT_e/m)^{1/2}$)											
-0.983	0.572	0.614	0.649	0.738	0.831	0.958	1.105	1.260	1.630	2.001	2.521	3.024
-0.931	0.571	0.600	0.638	0.719	0.821	0.934	1.056	1.204	1.547	1.886	2.365	2.848
-0.862	0.569	0.604	0.637	0.704	0.788	0.893	1.005	1.138	1.436	1.751	2.190	2.610
-0.793	0.568	0.597	0.629	0.691	0.773	0.851	0.943	1.059	1.332	1.618	2.007	2.401
-0.724	0.566	0.594	0.618	0.681	0.737	0.822	0.905	0.995	1.230	1.482	1.825	2.200
-0.655	0.570	0.590	0.611	0.667	0.719	0.774	0.845	0.929	1.129	1.361	1.666	1.987
-0.586	0.568	0.593	0.612	0.652	0.692	0.744	0.799	0.867	1.035	1.221	1.507	1.764
-0.517	0.570	0.586	0.609	0.637	0.679	0.710	0.751	0.813	0.945	1.102	1.325	1.568
-0.448	0.564	0.579	0.594	0.628	0.657	0.678	0.712	0.750	0.871	0.995	1.188	1.377
-0.379	0.572	0.584	0.595	0.620	0.628	0.654	0.674	0.707	0.787	0.894	1.038	1.175
-0.310	0.571	0.579	0.588	0.603	0.617	0.626	0.642	0.662	0.735	0.812	0.912	1.020
-0.241	0.571	0.579	0.580	0.596	0.601	0.605	0.606	0.618	0.659	0.723	0.815	0.934
-0.172	0.566	0.580	0.581	0.578	0.583	0.579	0.577	0.572	0.603	0.640	0.703	0.758
-0.103	0.565	0.571	0.571	0.575	0.563	0.551	0.542	0.536	0.550	0.576	0.613	0.668
-0.034	0.563	0.570	0.564	0.559	0.545	0.535	0.509	0.501	0.500	0.508	0.525	0.541
0.034	0.571	0.564	0.566	0.548	0.537	0.514	0.487	0.470	0.447	0.450	0.455	0.467
0.103	0.565	0.563	0.555	0.541	0.513	0.495	0.463	0.433	0.412	0.393	0.383	0.382
0.172	0.566	0.560	0.553	0.531	0.503	0.470	0.442	0.408	0.364	0.347	0.335	0.316
0.241	0.562	0.559	0.545	0.529	0.499	0.459	0.420	0.383	0.334	0.304	0.278	0.262
0.310	0.570	0.554	0.544	0.520	0.480	0.446	0.402	0.360	0.294	0.265	0.240	0.212
0.379	0.566	0.556	0.538	0.506	0.469	0.431	0.383	0.336	0.276	0.233	0.196	0.173
0.448	0.568	0.547	0.532	0.492	0.461	0.417	0.370	0.321	0.237	0.202	0.168	0.141
0.517	0.566	0.544	0.528	0.488	0.446	0.404	0.357	0.306	0.225	0.174	0.139	0.113
0.586	0.569	0.543	0.523	0.487	0.443	0.393	0.347	0.292	0.198	0.153	0.117	0.091
0.655	0.570	0.549	0.518	0.474	0.434	0.381	0.334	0.281	0.188	0.131	0.095	0.072
0.724	0.567	0.538	0.516	0.467	0.417	0.372	0.321	0.272	0.174	0.116	0.079	0.057
0.793	0.566	0.545	0.510	0.461	0.411	0.361	0.317	0.266	0.163	0.105	0.063	0.043
0.862	0.568	0.536	0.506	0.453	0.402	0.358	0.307	0.265	0.168	0.104	0.058	0.036
0.931	0.570	0.534	0.508	0.449	0.399	0.349	0.303	0.261	0.167	0.099	0.055	0.032
0.983	0.563	0.532	0.496	0.438	0.392	0.348	0.295	0.260	0.172	0.105	0.063	0.036

Table 5: Dependence of ion flux to the sphere on flow velocity and angle when $T_i = 1.0ZT_e$.

$v_f:$ $\cos \theta$	0.000	0.100	0.200	0.400	0.600	0.800	1.000	1.200	1.600	2.000	2.500	3.000
	Ion Flux density, Γ ($/n_{i\infty}(ZT_e/m)^{1/2}$)											
-0.983	0.618	0.678	0.721	0.808	0.914	1.041	1.169	1.319	1.647	2.028	2.519	3.032
-0.931	0.631	0.663	0.698	0.791	0.899	1.014	1.137	1.282	1.580	1.923	2.389	2.877
-0.862	0.626	0.660	0.703	0.778	0.872	0.972	1.093	1.206	1.477	1.790	2.206	2.655
-0.793	0.623	0.659	0.690	0.772	0.850	0.946	1.036	1.150	1.382	1.659	2.046	2.435
-0.724	0.621	0.649	0.679	0.750	0.818	0.901	0.985	1.076	1.287	1.541	1.869	2.221
-0.655	0.624	0.639	0.674	0.734	0.801	0.866	0.933	1.025	1.202	1.412	1.697	2.006
-0.586	0.625	0.650	0.670	0.719	0.777	0.832	0.892	0.959	1.110	1.295	1.533	1.799
-0.517	0.624	0.646	0.666	0.711	0.756	0.804	0.854	0.906	1.023	1.173	1.380	1.608
-0.448	0.623	0.640	0.651	0.695	0.729	0.767	0.806	0.850	0.945	1.070	1.243	1.407
-0.379	0.626	0.640	0.653	0.680	0.707	0.736	0.772	0.803	0.873	0.973	1.102	1.227
-0.310	0.629	0.633	0.650	0.667	0.702	0.714	0.736	0.756	0.799	0.882	0.983	1.085
-0.241	0.623	0.640	0.642	0.653	0.674	0.688	0.692	0.712	0.742	0.801	0.885	0.979
-0.172	0.627	0.637	0.637	0.649	0.663	0.660	0.668	0.670	0.682	0.720	0.777	0.842
-0.103	0.625	0.630	0.634	0.633	0.635	0.638	0.638	0.636	0.636	0.655	0.686	0.737
-0.034	0.624	0.618	0.623	0.620	0.618	0.613	0.602	0.595	0.578	0.592	0.602	0.612
0.034	0.626	0.627	0.615	0.613	0.606	0.587	0.571	0.562	0.538	0.529	0.535	0.539
0.103	0.614	0.614	0.615	0.599	0.586	0.568	0.547	0.532	0.495	0.466	0.461	0.444
0.172	0.620	0.611	0.607	0.591	0.572	0.548	0.524	0.501	0.449	0.423	0.401	0.391
0.241	0.616	0.613	0.601	0.573	0.562	0.532	0.502	0.470	0.413	0.373	0.344	0.312
0.310	0.626	0.605	0.596	0.568	0.538	0.516	0.477	0.450	0.379	0.340	0.296	0.272
0.379	0.619	0.599	0.586	0.559	0.532	0.493	0.458	0.424	0.356	0.297	0.260	0.226
0.448	0.622	0.597	0.585	0.550	0.513	0.470	0.443	0.401	0.324	0.277	0.219	0.185
0.517	0.623	0.601	0.579	0.537	0.499	0.471	0.418	0.379	0.302	0.238	0.188	0.147
0.586	0.618	0.597	0.575	0.525	0.488	0.448	0.404	0.364	0.277	0.218	0.163	0.123
0.655	0.624	0.593	0.563	0.520	0.471	0.432	0.390	0.345	0.259	0.191	0.133	0.103
0.724	0.626	0.599	0.562	0.519	0.467	0.417	0.376	0.323	0.246	0.178	0.117	0.082
0.793	0.620	0.592	0.558	0.507	0.456	0.402	0.363	0.319	0.235	0.164	0.104	0.067
0.862	0.623	0.587	0.554	0.492	0.448	0.395	0.344	0.305	0.221	0.152	0.094	0.055
0.931	0.625	0.586	0.552	0.485	0.431	0.386	0.334	0.292	0.208	0.144	0.086	0.051
0.983	0.620	0.588	0.562	0.478	0.433	0.370	0.331	0.288	0.213	0.143	0.083	0.045

Table 6: Dependence of ion flux to the sphere on flow velocity and angle when $T_i = 2.0ZT_e$.

v_f : $\cos \theta$	0.000	0.100	0.200	0.400	0.600	0.800	1.000	1.200	1.600	2.000	2.500	3.000
	Ion Flux density, Γ ($/n_{i\infty}(ZT_e/m)^{1/2}$)											
-0.966	0.707	0.755	0.797	0.901	1.009	1.113	1.247	1.382	1.674	1.990	2.444	2.899
-0.897	0.716	0.758	0.801	0.887	0.982	1.075	1.182	1.311	1.569	1.876	2.272	2.671
-0.828	0.727	0.752	0.789	0.868	0.962	1.049	1.150	1.260	1.487	1.745	2.094	2.485
-0.759	0.717	0.747	0.786	0.857	0.925	1.019	1.100	1.201	1.413	1.624	1.953	2.279
-0.690	0.722	0.744	0.779	0.841	0.928	0.988	1.067	1.127	1.324	1.516	1.797	2.083
-0.621	0.719	0.747	0.768	0.839	0.887	0.943	1.012	1.093	1.232	1.406	1.656	1.894
-0.552	0.723	0.749	0.765	0.805	0.870	0.918	0.983	1.048	1.203	1.310	1.511	1.743
-0.483	0.714	0.741	0.751	0.804	0.842	0.896	0.944	0.994	1.084	1.222	1.396	1.536
-0.414	0.716	0.737	0.756	0.788	0.844	0.859	0.900	0.936	1.025	1.109	1.237	1.410
-0.345	0.718	0.726	0.751	0.783	0.803	0.835	0.875	0.896	0.973	1.045	1.143	1.246
-0.276	0.712	0.728	0.746	0.763	0.785	0.803	0.822	0.866	0.889	0.950	1.027	1.089
-0.207	0.715	0.722	0.729	0.748	0.762	0.769	0.791	0.812	0.835	0.872	0.925	0.981
-0.138	0.716	0.717	0.728	0.745	0.744	0.753	0.755	0.768	0.780	0.808	0.830	0.865
-0.069	0.719	0.721	0.721	0.726	0.734	0.733	0.730	0.730	0.747	0.723	0.738	0.727
0.000	0.710	0.716	0.717	0.710	0.727	0.713	0.688	0.678	0.669	0.674	0.647	0.641
0.069	0.721	0.720	0.712	0.706	0.686	0.672	0.672	0.667	0.644	0.600	0.600	0.583
0.138	0.711	0.707	0.709	0.678	0.686	0.657	0.650	0.632	0.580	0.554	0.523	0.479
0.207	0.722	0.710	0.699	0.690	0.653	0.633	0.609	0.595	0.554	0.501	0.456	0.436
0.276	0.716	0.701	0.698	0.661	0.635	0.618	0.600	0.559	0.492	0.459	0.407	0.359
0.345	0.707	0.706	0.685	0.665	0.631	0.593	0.554	0.533	0.496	0.408	0.350	0.307
0.414	0.721	0.694	0.697	0.648	0.618	0.569	0.544	0.507	0.427	0.387	0.310	0.249
0.483	0.717	0.688	0.665	0.628	0.586	0.563	0.517	0.482	0.402	0.335	0.268	0.237
0.552	0.710	0.691	0.680	0.640	0.587	0.532	0.490	0.446	0.385	0.311	0.256	0.208
0.621	0.721	0.694	0.649	0.619	0.565	0.514	0.480	0.427	0.352	0.293	0.212	0.168
0.690	0.720	0.675	0.660	0.603	0.556	0.517	0.451	0.415	0.331	0.250	0.188	0.150
0.759	0.711	0.681	0.654	0.588	0.543	0.484	0.437	0.390	0.309	0.236	0.165	0.105
0.828	0.709	0.684	0.654	0.578	0.519	0.466	0.420	0.375	0.289	0.221	0.154	0.113
0.897	0.714	0.677	0.647	0.574	0.522	0.459	0.403	0.355	0.273	0.198	0.139	0.092
0.966	0.711	0.677	0.632	0.558	0.495	0.436	0.389	0.343	0.254	0.187	0.123	0.079

Table 7: Dependence of ion flux to the sphere on flow velocity and angle when $T_i = 5.0ZT_e$.

v_f : $\cos \theta$	0.000	0.200	0.400	0.600	0.800	1.000	1.500	2.000	2.500	3.000	4.000	5.000
	Ion Flux density, Γ ($/n_{i\infty}(ZT_e/m)^{1/2}$)											
-0.966	0.990	1.074	1.167	1.287	1.387	1.503	1.830	2.190	2.569	2.975	3.848	4.799
-0.897	0.986	1.075	1.145	1.245	1.359	1.460	1.759	2.069	2.422	2.784	3.611	4.443
-0.828	0.989	1.068	1.158	1.240	1.327	1.461	1.689	1.973	2.268	2.612	3.344	4.115
-0.759	0.991	1.043	1.124	1.222	1.304	1.380	1.608	1.879	2.184	2.458	3.089	3.754
-0.690	0.984	1.066	1.119	1.178	1.269	1.348	1.555	1.761	2.011	2.264	2.790	3.460
-0.621	1.007	1.043	1.098	1.166	1.237	1.316	1.474	1.689	1.886	2.107	2.634	3.119
-0.552	0.993	1.031	1.099	1.135	1.207	1.261	1.425	1.582	1.774	1.967	2.386	2.823
-0.483	1.003	1.048	1.072	1.126	1.174	1.241	1.331	1.506	1.673	1.825	2.135	2.553
-0.414	0.975	1.035	1.039	1.097	1.129	1.197	1.314	1.440	1.516	1.664	1.939	2.229
-0.345	0.989	1.009	1.048	1.080	1.124	1.141	1.246	1.316	1.447	1.537	1.729	1.973
-0.276	0.998	1.016	1.047	1.069	1.084	1.122	1.181	1.278	1.320	1.395	1.562	1.759
-0.207	0.993	0.999	1.012	1.044	1.076	1.100	1.133	1.180	1.229	1.293	1.386	1.514
-0.138	0.988	1.002	1.007	1.024	1.036	1.043	1.073	1.099	1.128	1.150	1.226	1.268
-0.069	0.978	1.009	0.997	0.998	1.014	1.025	1.024	1.025	1.077	1.063	1.086	1.103
0.000	0.999	0.976	0.980	0.973	0.973	0.993	0.973	0.987	0.968	0.945	0.950	0.986
0.069	0.983	0.987	0.976	0.965	0.950	0.959	0.947	0.899	0.886	0.883	0.832	0.771
0.138	0.989	0.952	0.964	0.952	0.936	0.921	0.869	0.842	0.819	0.772	0.706	0.639
0.207	0.985	0.972	0.931	0.946	0.900	0.887	0.854	0.794	0.736	0.692	0.645	0.563
0.276	0.984	0.951	0.928	0.884	0.890	0.855	0.795	0.748	0.678	0.642	0.510	0.437
0.345	1.003	0.939	0.944	0.898	0.858	0.848	0.777	0.686	0.618	0.537	0.475	0.442
0.414	0.989	0.943	0.894	0.871	0.847	0.804	0.710	0.633	0.562	0.499	0.370	0.337
0.483	0.981	0.950	0.906	0.853	0.806	0.782	0.691	0.601	0.531	0.438	0.319	0.264
0.552	0.980	0.921	0.871	0.856	0.780	0.752	0.642	0.555	0.458	0.392	0.277	0.208
0.621	1.011	0.930	0.854	0.815	0.785	0.733	0.617	0.514	0.438	0.344	0.243	0.175
0.690	0.983	0.905	0.876	0.797	0.746	0.706	0.593	0.484	0.377	0.310	0.205	0.150
0.759	0.981	0.924	0.833	0.772	0.730	0.672	0.544	0.441	0.366	0.271	0.154	0.096
0.828	0.983	0.900	0.834	0.768	0.709	0.650	0.516	0.411	0.311	0.241	0.149	0.083
0.897	0.984	0.893	0.815	0.749	0.685	0.628	0.495	0.379	0.284	0.218	0.120	0.063
0.966	0.996	0.899	0.825	0.732	0.661	0.603	0.475	0.356	0.271	0.187	0.101	0.050

Table 8: Dependence of ion flux to the sphere on flow velocity and angle when $T_i = 10.ZT_e$.

v_f : $\cos \theta$	0.000	0.200	0.400	0.600	0.800	1.000	1.500	2.000	2.500	3.000	4.000	5.000
	Ion Flux density, Γ ($/n_{i\infty}(ZT_e/m)^{1/2}$)											
-0.966	1.338	1.417	1.505	1.633	1.742	1.840	2.136	2.484	2.816	3.204	4.018	4.904
-0.897	1.326	1.410	1.515	1.588	1.697	1.802	2.077	2.369	2.696	3.023	3.758	4.542
-0.828	1.322	1.410	1.492	1.588	1.658	1.755	2.005	2.264	2.555	2.874	3.508	4.251
-0.759	1.325	1.389	1.476	1.540	1.652	1.721	1.932	2.180	2.435	2.698	3.294	3.924
-0.690	1.321	1.385	1.466	1.543	1.585	1.660	1.917	2.106	2.309	2.568	3.079	3.625
-0.621	1.338	1.389	1.457	1.510	1.567	1.644	1.788	1.990	2.191	2.400	2.816	3.355
-0.552	1.355	1.379	1.446	1.486	1.560	1.588	1.753	1.924	2.091	2.273	2.628	3.010
-0.483	1.316	1.372	1.419	1.478	1.504	1.563	1.716	1.843	1.975	2.129	2.450	2.801
-0.414	1.306	1.353	1.407	1.448	1.487	1.522	1.648	1.736	1.864	2.015	2.266	2.512
-0.345	1.348	1.359	1.408	1.420	1.455	1.487	1.561	1.675	1.750	1.860	2.079	2.320
-0.276	1.303	1.343	1.351	1.404	1.421	1.460	1.517	1.586	1.681	1.725	1.879	2.011
-0.207	1.331	1.341	1.369	1.400	1.426	1.411	1.477	1.520	1.560	1.644	1.726	1.871
-0.138	1.323	1.347	1.358	1.344	1.370	1.371	1.434	1.450	1.486	1.512	1.581	1.657
-0.069	1.319	1.322	1.328	1.339	1.348	1.372	1.343	1.359	1.382	1.404	1.421	1.451
0.000	1.335	1.337	1.326	1.321	1.320	1.303	1.311	1.354	1.309	1.285	1.314	1.294
0.069	1.322	1.301	1.305	1.308	1.295	1.270	1.262	1.229	1.228	1.212	1.150	1.117
0.138	1.303	1.316	1.317	1.305	1.269	1.265	1.216	1.193	1.137	1.119	1.052	1.007
0.207	1.350	1.316	1.298	1.265	1.247	1.205	1.201	1.116	1.090	1.028	0.931	0.855
0.276	1.317	1.294	1.269	1.248	1.226	1.192	1.112	1.064	1.000	0.946	0.819	0.720
0.345	1.329	1.287	1.285	1.242	1.191	1.168	1.102	1.003	0.950	0.863	0.783	0.662
0.414	1.315	1.264	1.229	1.222	1.182	1.139	1.020	0.980	0.888	0.784	0.646	0.529
0.483	1.313	1.276	1.221	1.196	1.153	1.084	1.025	0.902	0.810	0.750	0.576	0.475
0.552	1.312	1.245	1.208	1.178	1.127	1.091	0.946	0.843	0.745	0.681	0.524	0.401
0.621	1.341	1.282	1.208	1.151	1.101	1.049	0.907	0.810	0.715	0.595	0.445	0.329
0.690	1.315	1.247	1.182	1.123	1.066	1.013	0.901	0.767	0.650	0.579	0.397	0.297
0.759	1.326	1.248	1.184	1.097	1.039	0.995	0.845	0.721	0.623	0.500	0.340	0.223
0.828	1.325	1.254	1.164	1.103	1.016	0.958	0.814	0.688	0.560	0.472	0.315	0.207
0.897	1.317	1.224	1.166	1.080	1.008	0.929	0.784	0.644	0.533	0.425	0.265	0.171
0.966	1.328	1.229	1.149	1.070	0.980	0.914	0.737	0.602	0.489	0.384	0.230	0.136